

Development of a Finite Element-Based Hall-Thruster Model

Subrata Roy* and B. P. Pandey†
Kettering University, Flint, Michigan 48504

This paper aims to characterize the Hall-thruster plasma dynamics in the framework of multifluid model. Effect of the ionization and the recombination has been included in the present model. Based on the experimental data, a third-order polynomial in electron temperature is used to calculate the ionization rate. The neutral dynamics is included only through the neutral continuity equation in the presence of a uniform neutral flow. The electrons are modeled as magnetized and hot, whereas ions are assumed unmagnetized and cold. The computed plasma density profile shows that the location of the density maximum is shifted slightly inward from the channel exit. This suggests that the maximum ionization takes place inside the channel. This is in conformity with the experimental observations. The maximum electron temperature increase takes place just near the exit closer to the inner wall. This is consistent with the electron gyration velocity distribution. The plasma potential is fairly flat in most parts of the channel before falling at the exit. Simulation results are interpreted in the light of experimental observations and available numerical solutions in the literature.

Nomenclature

B, \mathbf{B}	= magnetic field, G
E, \mathbf{E}	= electric field, V/m
E_i	= ionization potential
e	= electron charge, C
j, J	= current, mA
L	= differential operator
M	= mass matrix
m	= mass, kg
N	= basis function
n	= number density, m^{-3}
R	= solution residual
r	= radial direction
S	= Assembly operator
T	= temperature, eV
t	= time, s
u, \mathbf{U}	= state variable
V, \mathbf{V}	= velocity, m/s
w	= weight function
Z	= ionicity
z	= axial direction
Γ	= flux of the propellant, $m^{-2}s^{-1}$
Δ	= step
ϑ	= implicitness
ν	= collision frequency
σ	= ionization cross section, m^2
ϕ	= potential, V
Ω	= solution domain

Subscripts

c	= charge exchange
d	= discharge
e	= electron
el	= element
H	= Hall current

i	= ion
k	= degree of interpolation polynomial
n	= neutrals
r	= radial component
t	= thermal velocity
z	= axial component
α	= electron or ion
θ	= azimuthal component
τ	= time-stepping index
$*, 0$	= reference value

Superscripts

h	= discretization
p	= iteration index
0	= neutrals
$+$	= singly ionized
$++$	= doubly ionized

I. Introduction

HALL-THRUSTER, also known as closed-drift thruster, experimentation started in the early 1960s, and because of a diligent Russian effort became an enabling technology for onboard propulsion in many low-Earth-orbit and geosynchronous satellites.¹ The term “closed drift” refers to the azimuthal drift of electrons that is common to variants of such thrusters, for example, stationary plasma thruster (SPT), thruster with anode layer, etc. The SPT thruster is a coaxial device that consists of four main parts: the anode, which serves as a propellant distributor; an annular acceleration channel made of boron nitride; a magnetic unit; and a hollow cathode (Fig. 1). The plasma column is contained within two coaxial dielectric cylinders that constitute the discharge channel, with the anode at one end of the channel and the exit at the other end of the channel. The discharge is created between the anode of the thruster and an external hollow cathode located downstream of the channel exit. The magnetic system consists of a series of electromagnetic coils employed inside the inner cylinder and outside the outer cylinder and predominantly radial field with a maximum just upstream of the channel exit. The electrons from the cathode enter the chamber and are subject to azimuthal $\mathbf{E} \times \mathbf{B}$ drift. The electrons in the closed drift undergo ionizing collisions with the propellant gas. Although the magnetic field is strong enough to capture electrons in an azimuthal drift, it is not strong enough to contain the resulting ions, which are essentially accelerated by the imposed axial electric field. The suppression of axial electron mobility by the imposed radial field, while leaving ion mobility unaffected, enables the plasma to support an electric field with a potential difference close to the applied

Received 29 April 2002; revision received 6 September 2002; accepted for publication 9 May 2003. Copyright © 2003 by Subrata Roy and B. P. Pandey. Published by the American Institute of Aeronautics and Astronautics, Inc., with permission. Copies of this paper may be made for personal or internal use, on condition that the copier pay the \$10.00 per-copy fee to the Copyright Clearance Center, Inc., 222 Rosewood Drive, Danvers, MA 01923; include the code 0748-4658/03 \$10.00 in correspondence with the CCC.

*Director, Computational Plasma Dynamics Laboratory and Associate Professor of Mechanical Engineering, 1700 West Third Avenue; sroy@kettering.edu. Associate Fellow AIAA.

†Postdoctoral Research Associate, Computational Plasma Dynamics Laboratory, 1700 West Third Avenue; bpandey@kettering.edu. Member AIAA.

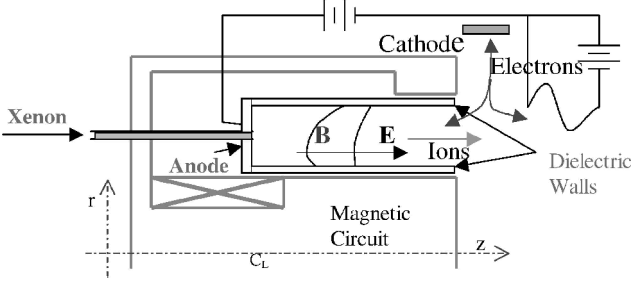


Fig. 1 Half-plane schematic of a single-stage stationary plasma thruster.

voltage. The ions are accelerated to kinetic energies within 80% of the applied discharge voltage.²

Present-day Hall thrusters offer specific impulses over 1600 s, thrust over 80 mN, and power exceeding 1.5 kW at efficiencies of about 50%. The commercial exploitation of Hall thrusters imposes a stringent constraint of trouble-free operation for more than 8000 hrs.³ The physics inside the Hall thruster has to be reasonably well understood in order to make any significant change in efficiency without compromising the lifetime. This is a challenge, as the choice of thruster size requires an optimum selection between efficiency and lifetime.⁴ Despite significant numerical and theoretical advances of the recent past, we lack an adequate numerical model to describe critical regions of a Hall-thruster plasma dynamics in a self-consistent fashion.^{5,6}

Numerical simulation of the plasma dynamics of a Hall thruster has been carried out recently by several authors in the framework of the hybrid as well as the fluid models.^{7–27} The one-dimensional fluid model of the partially ionized plasma incorporating the neutral dynamics and the effect of the plasma-wall interaction has been documented recently.^{25–27} This present study extends the two-dimensional, two-fluid, fully ionized thruster plasma model of Roy and Pandey²² to a two-dimensional, three-fluid, partially ionized plasma model in order to investigate the effect of ionization and recombination on the dynamics of the Hall thruster. The neutral dynamics is included in the present work because without neutral dynamics the effect of ionization and recombination cannot be studied satisfactorily. The self-consistent two-dimensional, three-fluid formulation of the bounded thruster plasma is the novel feature of the present work. To the best of our knowledge, such a simulation has not been reported in the literature.

Numerical novelty includes the utilization of subgrid embedded (SGM) finite elements,^{28,29} for convergence and stability of the solution. It is based on a nonlinear, nonhierarchical, high-degree Lagrange finite element basis for use in a discretized approximation. SGM elements utilize local mesh, velocity and diffusion parameters to modify the dissipative flux-vector (second-derivative) terms in the equation. For the hyperbolic equation a second-derivative artificial diffusion term with a vanishing coefficient is added. The theory employs element-level static condensation and eigenvalue analysis for efficiency, nodal-rank homogeneity, and essentially nonoscillatory solution. Unlike traditional upwind methods, however, nonlinear SGM does not introduce any unnecessary diffusion to distort the solution.

The numerical model and the simulation results are presented in the subsequent sections. In Sec. II we discuss pertinent theoretical issues. In Sec. III the solution algorithm is described. The numerical results are documented in Sec. IV. Finally, Sec. V contains conclusions and future work.

II. Theoretical Issues

The dynamics of a partially ionized, thruster plasma is quite complicated,^{1–3,7–12,15,17–20,26,27} as several elastic and inelastic processes can occur simultaneously. However, not all processes are equally probable. For example, momentum exchange between electron-electron and ion-ion will not be important in comparison with the electron-ion momentum exchange as the relative drift

between similar particles is small in comparison with the drift between electrons and ions. The collisions between electron-neutral, electron-ion, and ion-neutral play an important role. The plasma-neutral collision usually determines the kinetics of the motion.

The rate of the ion production in plasma is determined by the ionization frequency. The ionization rate is given as

$$S_{\text{ioniz}} = n_e n_n \langle V_{\text{eth}} \sigma_i(V_{\text{eth}}) \rangle = k_i n_e n_n \quad (1)$$

where σ_i is the total cross section of the process, n_e is the electron number density, and process constant $k_i = \langle \sigma_i(V_{\text{eth}}) V_{\text{eth}} \rangle$, with the averaging done over the velocities of the electrons. A general electron temperature-dependent empirical formula can be fitted to the ionization process constant $k_i = [k_i^{0+}, k_i^{0++}, k_i^{I++}]$, corresponding to $\text{Xe}^0 \rightarrow \text{Xe}^+$, $\text{Xe}^0 \rightarrow \text{Xe}^{++}$, and $\text{Xe}^+ \rightarrow \text{Xe}^{++}$ processes, where Xe is Xenon. We shall use the following generalized process rate that is a sum of all three ionization rates²⁶:

$$k_i = (-3.2087 \times 10^{-5} T_e^3 - 0.0022 T_e^2 + 0.7101 T_e - 1.76) \times 10^{-14} \quad (2)$$

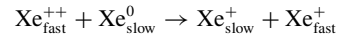
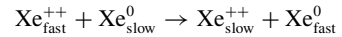
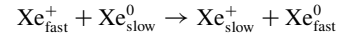
Electron-ion collisions on the other hand can lead to recombination. The rate of recombination is given as

$$S_{\text{recom}} = -n_e n_i \langle V_{\text{eth}} \sigma_{ei}(V_{\text{eth}}) \rangle = -\alpha n_e n_i \quad (3)$$

where recombination coefficient α can be approximated as³⁰

$$\alpha = 1.09 \times 10^{-20} n_e T_e^{-\frac{9}{2}} \text{ m}^3/\text{s} \quad (4)$$

Slow propellant ions are created as a result of resonant charge-exchange collisions of the following types between the fast “beam” (current) ions and slow thermal neutrals:



The collisional cross section for the preceding processes are comparable³¹ $\sigma(\text{Xe} - \text{Xe}^+) \sim 4.38 \times 10^{-19} \text{ m}^2$ and $\sigma(\text{Xe} - \text{Xe}^{++}) \sim 4.98 \times 10^{-19} \text{ m}^2$. Thus, it would appear that all of the preceding processes are equally important. However, in the last process stripping of an electron is involved, the energy required exceed 1 keV (Ref. 32), and, thus, the last process is ignored. The cross section for $\text{Xe}-\text{Xe}^+$ for example is given by³³

$$\sigma(\text{Xe} - \text{Xe}^+) = [a - b \log_{10}(\Delta u)](E_i/E_H)^{-1.5} \times 10^{-20} \text{ m}^2 \quad (5)$$

where $a = 181$, $b = 21.2$, $E_i = 12.13 \text{ eV}$, xenon ionization potential, and $E_H = 13.6 \text{ eV}$, hydrogen ionization potential. For a relative velocity Δu between 10 and $2 \times 10^3 \text{ m/s}$, the charge-exchange cross section varies between 10^{-20} to 10^{-19} m^2 .

Having delineated some of the important physical processes in the partially ionized thruster plasma, we shall now give the basic set of equations that describes the dynamics of the process under investigation. We shall assume that the ions are unmagnetized because for typical parameters of a thruster plasma, namely, magnetic field $B \sim 200 \text{ G}$ and ion velocity $4 \times 10^3 \text{ m/s}$, the gyration radius of ions is about 0.1 m, which is much larger than the size of the thruster (0.02–0.03 m). In the present simulation the maximum value of magnetic field, near the exit, is 242 G. Therefore, the effect of magnetic field on the ion transport will be ignored. Further, the pressure term in the ion momentum equation can be ignored as the thermal energy of the ions is much smaller than their kinetic energy, that is, $T_i \ll m_i V_i^2$. Owing to the small inertia, electron-responsetime is much faster than the ion-responsetime. As a result, electrons will attain the steady state faster than the ions. Keeping this in mind, electron momentum and energy equations are solved at steady state, whereas for ions and neutrals a set of time-dependent continuity and momentum equations are simultaneously solved.

An annular cylinder can adequately characterize Hall-thruster geometry. Ignoring any variation in the azimuthal θ direction, we shall take a two-dimensional axisymmetric r, z representation of the thruster. The following set of equations written in the component form is used to describe the dynamics of thruster plasma with the azimuthal ion velocity $V_{i\theta}$, and dependence on the azimuthal angle $\partial/\partial\theta$ set to zero. The continuity equation for the electron and the ions are

$$\frac{\partial n_\alpha}{\partial t} + \frac{1}{r} \frac{\partial}{\partial r}(r n_\alpha V_{\alpha r}) + \frac{\partial(n_\alpha V_{\alpha z})}{\partial z} = S \quad (6)$$

where $S = S_{\text{ioniz}} - S_{\text{recomb}}$. Assuming that the neutral velocity has axial component only, the neutral continuity equation is

$$\frac{\partial n_n}{\partial t} + \frac{\partial(n_n V_{nz})}{\partial z} = S_{\text{recomb}} - k_i^{0+} n_e n_n - k_i^{0++} n_e n_n \quad (7)$$

The right-hand side of the continuity equations (6–7) represents source and sink term caused by ionization and recombination. The sink term of the neutral continuity equation (7) is slightly different than the ionization source term of the plasma continuity equation (6) because of the presence of the processes like $\text{Xe}^+ \rightarrow \text{Xe}^{++}$ in the S_{ioniz} .

The ion momentum equations are,

$$\begin{aligned} \frac{\partial V_{ir}}{\partial t} + V_{ir} \frac{\partial V_{ir}}{\partial r} + V_{iz} \frac{\partial V_{ir}}{\partial z} = & -\frac{T_i}{m_i n_i} \frac{\partial n_i}{\partial r} + \left(\frac{Ze}{m_i}\right) E_r - \nu_c V_{ir} \\ & + \left(\frac{m_e}{m_i}\right) \nu_{ei}(V_{er} - V_{ir}) - 0.5 \nu_{in}(V_{ir} - V_{nr}) + \left(\frac{S}{n_i}\right) V_{ir} \end{aligned} \quad (8)$$

$$\begin{aligned} \frac{\partial V_{iz}}{\partial t} + V_{ir} \frac{\partial V_{iz}}{\partial r} + V_{iz} \frac{\partial V_{iz}}{\partial z} = & -\frac{T_i}{m_i n_i} \frac{\partial n_i}{\partial z} + \left(\frac{Ze}{m_i}\right) E_z - \nu_c V_{iz} \\ & + \left(\frac{m_e}{m_i}\right) \nu_{ei}(V_{ez} - V_{iz}) - 0.5 \nu_{in}(V_{iz} - V_{nz}) + \left(\frac{S}{n_i}\right) V_{iz} \end{aligned} \quad (9)$$

The factor 0.5 before ion–neutral collision term comes from reduced mass $m_i m_n / (m_i + m_n) \approx m_i / 2$. The electron momentum equations are

$$\begin{aligned} V_{er} \frac{\partial V_{er}}{\partial r} + V_{ez} \frac{\partial V_{er}}{\partial z} - \frac{V_\theta^2}{r} = & \frac{1}{m_e n_e} \frac{\partial n_e T_e}{\partial r} \frac{e}{m_e} (E_r + V_{e\theta} B_z) \\ & - \nu_{ei}(V_{er} - V_{ir}) - \nu_{en}(V_{er} - V_{nr}) + \left(\frac{S}{n_e}\right) V_{er} \end{aligned} \quad (10)$$

$$\begin{aligned} V_{er} \frac{\partial V_{e\theta}}{\partial r} + V_{ez} \frac{\partial V_{e\theta}}{\partial z} + \frac{V_{er} V_{e\theta}}{r} = & \frac{e}{m_e} (V_{ez} B_r - V_{er} B_z) \\ & + \left(\frac{S}{n_e}\right) V_{e\theta} - (V_{ei} + V_{en}) V_{e\theta} \end{aligned} \quad (11)$$

$$\begin{aligned} V_{er} \frac{\partial V_{ez}}{\partial r} + V_{ez} \frac{\partial V_{ez}}{\partial z} = & -\frac{1}{m_e n_e} \frac{\partial n_e T_e}{\partial z} - \frac{e}{m_e} (E_z - V_{e\theta} B_r) \\ & - \nu_{ei}(V_{ez} - V_{iz}) - \nu_{en}(V_{ez} - V_{nz}) + \left(\frac{S}{n_e}\right) V_{ez} \end{aligned} \quad (12)$$

The electron energy equation is,

$$\begin{aligned} \frac{3}{2} \left(\frac{\partial T_e}{\partial t} + \mathbf{V}_e \cdot \nabla T_e \right) = & -T_e \nabla \cdot \mathbf{V}_e - \nu \{ V_{er}^2 + V_{e\theta}^2 + V_{ez}^2 \\ & + 2[V_{er}(V_{e\theta} + V_{ez}) + V_{ez} V_{e\theta}] \} + \nu_{ei}(V_{er} V_{ir} + V_{ez} V_{iz}) \\ & + \nu_{en}(V_{er} V_{nr} + V_{ez} V_{nz}) + 3 \frac{m_e}{m_i} \nu_{ei}(T_i - T_e) \\ & + 3 \frac{m_e}{m_n} \nu_{en}(T_n - T_e) + \frac{S}{n_e} \left(\frac{3}{2} T_e + \alpha E_i \right) \end{aligned} \quad (13)$$

where $\nu = \nu_{ei} + \nu_{en}$. In Eqs. (6–13), V_e, V_i are the electron and ion velocities, respectively; n_j is the number density of the j th particle with $j = e$ and i ; ν_{ei}, ν_{en} are the electron–ion and electron–neutral collision frequencies respectively; ν_c is the ion charge-exchange collision frequency; and the value of α is between (2–3).¹⁸ The electron dynamics are determined by the pressure gradient, electric and magnetic forces, and the collisional exchange of momentum in Eqs. (10–12). The convective term in these equations retains the effect of the electron inertia.

The contribution of the electron inertia is small, and on this basis, its effect on the plasma dynamics is generally ignored. However, in the regions of sharp flow gradients the effect of the convective term can become finite, and therefore the convective term is retained in this formulation. Similarly, because collision timescales are much slower than the electron–cyclotron gyration timescale one can ignore elastic and inelastic collision terms in comparison with the Lorentz force term $\mathbf{V} \times \mathbf{B}$ in the momentum equation. Such an approach will exclude the dynamics of the momentum exchange as well as the effect of ionization and recombination, severely limiting the applicability of the model to the thruster plasma. Therefore, all of the collision terms are retained in the electron momentum equations (10–12).

Equation (13) includes the effect of Joule heating, a contribution caused by exchange of random thermal energy and ionization and recombination. The simulation of Katz et al.¹⁴ shows that the average ion energy remains nearly constant in the channel. Therefore, we also assume in our model that the ion energy is constant.

In closure, Eqs. (6–13) are supplemented with the simple form of Ohm's law³⁴

$$\mathbf{E} \equiv -\nabla\phi = (m_e \nu_{ei}/e)(V_i - V_e) + (1/en_e) \nabla n_i T_i \quad (14)$$

Equation (14) yields the relationship between the current and strength of the electric field in the plasma. The electric field has been written in the moving frame of the plasma, that is, $\mathbf{E} \equiv \mathbf{E}' + \mathbf{V} \times \mathbf{B}$.

Before numerically solving the preceding set of equations (6–14), we normalize the physical variables as follows. Temperature T is normalized using the first ionization potential of Xenon $T_* = E_i = 12.1$ eV. All other dependent variables can be normalized from

$$V_* = \sqrt{T_*/m_i} = 2 \times 10^3 \text{ m/s}, \quad n_* = \Gamma_*/V_* = 0.5 \times 10^{17} \text{ m}^{-3}$$

$$\nu_* = \sigma_* n_* V_* = \sigma_* \Gamma_* \simeq 2. \times 10^5 \text{ s}^{-1}$$

where

$$\sigma_* = \sigma_0 \sqrt{m_i/m_e}$$

The fundamental length scale l_0 is defined in terms of characteristic velocity and collisional frequency $l_0 = V_*/\nu_*$. The timescale is $t_0 = 1/\nu_*$.

To solve numerically the formulation (6–14), proper initial and boundary condition specifications are necessary to make the problem well posed. The axial velocities of electrons and ions are not fixed at the inlet. Under typical conditions, next to the anode, a plasma sheath (typical width \sim Debye length) forms, and ions must flow into the sheath from the quasi-neutral region. The axial velocity is near zero close to anode and then begins to rise at the edge of the acceleration zone, reaching a maximum velocity beyond the exit.²¹ Such flow behavior has also been observed in the classical nozzle problem, where flow changes smoothly from subsonic (in the narrow region) to supersonic flow in the divergent region. Therefore, a sonic point, where the flow velocity equals the characteristic speed of the medium, is always expected at the exit. We shall impose the choked-exit¹⁸ boundary condition for the ion axial velocity. Furthermore, axial electron flow will be assumed inward at the channel exit. We impose zero radial velocity for the electrons and ions at the inlet and leave it floating elsewhere. At the inlet the plasma density is equated to the reference value. The neutral density at the inlet depends upon the mass-flow rate. In the present calculation the mass-flow rate is $\sim 6 \text{ mg s}^{-1}$, a value relevant to a thruster operating at 1.5-kW power level.^{2,13} The corresponding neutral density is

$n_n \sim 10^{18} \text{ m}^{-3}$. The homogeneous Neumann condition is imposed on the electrostatic potential at the inlet. Because at the cathode the potential is zero, a vanishing potential is assumed at the outlet. For ion density a homogeneous Neumann condition is assumed. At the upstream boundary (thruster inlet plane) we specify an electron temperature of $T_e = 5 \text{ eV}$, which is close to the experimental data.^{5,24}

In a typical Hall-thruster experiment the radial magnetic field is dominant compared to the axial field. The radial magnetic field decreases from a typical maximum of about 200 G near the channel exit to a much lower value ($\sim 30\text{--}40 \text{ G}$) near the anode, though higher values of radial magnetic fields ($\sim 350 \text{ G}$) have been utilized recently for P5-class of thrusters.² The presence of this radial magnetic field inhibits electron flow to the anode and in the process considerably enhances the ionization caused by electron impact. In the presence of a very strong radial magnetic field and in the absence of any collision, the axial electron current can be completely inhibited. Thus, the current is mainly carried by the ions $j_z \approx j_i$. Assuming a quasineutral ($n_i \approx n_e$) plasma, the Hall current per unit radius is

$$J_H \approx en_e \int_0^r \left(\frac{E}{B} \right) dr \approx \frac{en_e \phi_d}{B} \quad (15)$$

where ϕ_d is the discharge potential. Note that the discharge potential is the sum of the column potential drop ϕ , the cathode fall potential, and the possible potential drop in the plasma region next to the exhaust and outside the cylinders. The corresponding Hall current density can be expressed as

$$j_H = en_e E/B \approx en_e E_z/B_r \quad (15a)$$

For $j_i \approx en_e V_i$ we have

$$J_H \approx j_i \phi_d / B V_i \approx j_i \sqrt{m_i \phi_d / 2e B^2} \quad (16)$$

where the maximum ion velocity is $V_i = (2e\phi_d/m_i)^{1/2}$. Clearly, for a given magnetic field, $J_H/j_i \sim \sqrt{\phi_d}$. For an efficient operating system current is carried by the ions, and ions attain maximum velocity. Thus we shall anticipate that the ensuing potential distribution (and the resultant accelerating electric field) will be in the region of maximum magnetic field strength.

III. Finite Element Based Modeling

This work is an extension of the multivariable design code development of Roy³⁵ and Balagangadhar and Roy.³⁶ Using L as a differential operator, a general formulation for Eqs. (6–14) can be expressed as $L(\mathbf{U}) = 0$, where $\mathbf{U} = \{n_\alpha, V_{iz}, V_{ir}, V_{ez}, V_{er}, V_{e\theta}, T_e, \phi\}^T$. The weak statement formed by multiplying $L(\mathbf{U})$ with an appropriate weighting function w and integrating over the computational domain (and thus weakening the continuity requirement of the finite element basis function²⁹) underlines the development of a range of computational-fluid-dynamics algorithms. Such an integral statement associated with Eqs. (6–14) is

$$\int_{\Omega} w L(\mathbf{U}) d\Omega = 0 \quad (17)$$

where w denotes any admissible test function.³⁵ Thereafter, the finite element (FE) spatial semidiscretization of the domain Ω of Eqs. (6–14) employs the mesh $\Omega^h = \cup_{\text{el}} \Omega_{\text{el}}$ and Ω_{el} is the generic computational domain where subscript el denotes a finite element. Using superscript h to denote spatial discretization, the FE weak statement implementation for Eq. (17) defines the approximation as

$$u(x_j) \approx u^h(x_j) = \bigcup_{\text{el}} u_{\text{el}}(x_j), \quad u_{\text{el}}(x_j) = N_k U_{\text{el}}$$

where the trial space FE basis set $N_k(x_j)$ typically contains Chebyshev, Lagrange, or Hermite interpolation polynomials complete to degree k , plus perhaps “bubble functions.”³⁵

The spatially semidiscrete FE implementation of the weak statement $W S^h$ for Eq. (17) leads to

$$W S^h = S_{\text{el}} \left[\int_{\Omega_{\text{el}}} N_k L_{\text{el}}(\mathbf{U}) d\tau \right] \quad (18)$$

S_{el} symbolizes the assembly operator carrying local (element) matrix coefficients into the global arrays. Application of Green–Gauss divergence theorem in Eq. (18) will yield natural homogenous Neumann boundary conditions and the surface integral that contains the unknown boundary fluxes wherever Dirichlet (fixed) boundary conditions are enforced.

Independent of the physical dimension of Ω , and for general forms of the flux vectors, the semidiscretized weak statement of Eq. (18) always yields an ordinary differential equation system:

$$\mathbf{M} \frac{d\mathbf{U}}{dt} + \mathbf{R}(\mathbf{U}) = \mathbf{0} \quad (19)$$

where $\mathbf{U}(t)$ is the time-dependent finite element nodal vector. The time derivative $d\mathbf{U}/dt$ is generally replaced with a ϑ -implicit or τ -step Runge–Kutta time-integration procedure. In Eq. (19), $\mathbf{M} = S_{\text{el}}(\mathbf{M}_{\text{el}})$ is the mass matrix associated with element-level interpolation, and \mathbf{R} carries the element convection information and the diffusion matrix resulting from genuine (non-Eulerian) or numerical elemental viscosity effects and all known data. Equation (19) is usually solved using a Newton–Raphson scheme²⁹:

$$\mathbf{U}_{\tau+1}^{i+1} = \mathbf{U}_{\tau+1}^i + \Delta \mathbf{U}^i = \mathbf{U}_{\tau} + \sum_{p=0}^i \mathbf{U}^{p+1}$$

where

$$\Delta \mathbf{U}^i = - \left[\mathbf{M} + \vartheta \Delta t \left(\frac{\partial \mathbf{R}}{\partial \mathbf{U}} \right) \right]^{-1} \mathbf{R}(\mathbf{U}) \quad (20)$$

In Eq. (20) ϑ is the implicitness of the numerical algorithm, and $0 < \vartheta < 1$. The obvious numerical issues will be associated with calculation of the Jacobian, $\partial \mathbf{R} / \partial \mathbf{U}$, and inversion of the $\mathbf{M} + \vartheta \Delta t (\partial \mathbf{R} / \partial \mathbf{U})$ matrix with sufficient accuracy. Equations (6–14) are strongly coupled, and the Jacobian matrix for this problem becomes very stiff for a realistic mass ratio of electron and ion. This results in solution divergence for a standard Galerkin finite element approach on a moderate to fine mesh. As a remedy, we utilized a high-order-accurate SGM finite element^{28,29} method to achieve a stable monotone solution on a relatively coarse grid. SGM elements use statically condensed higher-degree polynomial basis functions N_S for high solution fidelity.

The choice of time step is dictated by the Courant–Friedrich–Lewy condition.³⁷ The solution at any time step is declared convergent when the maximum residual for each of the state variables becomes smaller than a chosen convergence criterion of $\epsilon = 10^{-4}$. The steady state is declared when the preceding convergence criteria is met at the first iteration of any time step. Here, the convergence of a solution vector \mathbf{U} on node j is defined as the norm:

$$\frac{\|\mathbf{U}_j - \mathbf{U}_{j-1}\|}{\|\mathbf{U}_j\|} \leq \epsilon \quad (21)$$

IV. Numerical Results and Discussion

We recall that the thruster plasma is modeled by a two-dimensional axisymmetric (r - z) geometry. The θ direction is along the azimuth. We consider a two-dimensional magnetic field with radial and axial components, where the radial field is dominant (Fig. 2). The magnetic field lines near the exit close outside the thruster indicating that the near-plume region plasma will be affected by the presence of the magnetic field. However, the simulation domain in the present work corresponds only to the bounded region. Equation set (6–14) is solved using SGM finite elements on a biquadratic 9×9 mesh with 361 equidistant nodes. We have employed a trapezoidal

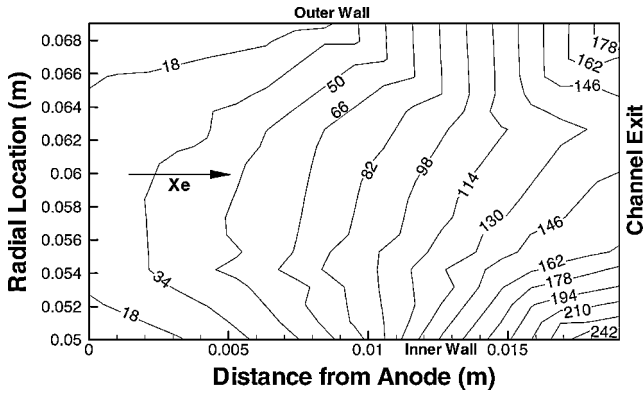


Fig. 2 Measured radial magnetic field in Gauss inside the thruster acceleration channel (Manzella, D., and Peterson, P., Private Communication, 2001).

time-stepping procedure, that is, $\vartheta = 0.5$ in Eq. (20), for this paper. In the present formulation the ion dynamics are time dependent, whereas electron dynamics have been assumed time independent. This is a plausible assumption because, owing to their small inertia, the electron will reach a steady state over the ion dynamic scale.⁹ The code uses variable time steps until the transient features die down and the iteration converges to a steady state. All solutions presented in this section have iterated to a steady state.

Figure 3a describes the neutral density contours. We use the reference values of physical parameters pertaining to a typical 1.5-kW class thruster that has a mass-flow rate $\sim 6 \text{ mg s}^{-1}$ corresponding to $n_n = 10^{18} \text{ m}^{-3}$. As is clear from the figure, neutral density is the highest at the inlet region and gradually decreases towards the channel exit. As ionization increases towards the exit (caused by an increase in the electron temperature), the neutral number density should decrease, and we see such a behavior. This is consistent with the fact that as a neutral enters the thruster chamber it undergoes impact ionization. Some experiment in the literature⁹ suggests that the minimum in neutral density is not necessarily correlated to the corresponding increase of the ion density. However, in the present work the plasma density prediction displays a correlation between ion and neutral number densities that is similar to the reported experimental data.^{2,5} We attribute this correlation to the temperature-dependent, self-consistent calculation of the ionization rate.

Figure 3b plots the plasma number density contours. The ion (electron) number density increases rapidly from a base value of 10^{17} m^{-3} and attains a maximum value $7 \times 10^{17} \text{ m}^{-3}$ upstream of the acceleration channel before decreasing near the exit. The experimental results^{2,13} show that the plasma density reaches its peak value inside the acceleration channel, near the inner wall before the exit plane. In this region the radial magnetic field is the maximum, and thus a large number of electrons are inhibited from moving in the axial direction, resulting in a high probability of impact ionization and plasma production. The maximum plasma density inside the acceleration channel agrees with the fact that the ionization channel is well inside the thruster. There is no significant effect of ionization and recombination on the plasma number density. This could have been anticipated on the grounds that in a Hall thruster, where the pressure is low and ion currents exceed the electron current, the effect of the ion production and loss to the ion continuity equation (6) is negligible.¹⁹

The experimental result for a 1.6-kW class thruster¹³ displays two distinct peaks in the ion number density profile located at about 0.02 and 0.032 m from the anode. These peaks are attributed to different ionization mechanisms—to the electron thermal energy upstream (0.02 m) and to the availability of electron gyration energy at 0.032 m. These results underline the complexity of the thruster plasma dynamics and inadequacies of the existing numerical models. Several important questions need to be addressed in order to explain the physical mechanism behind the experimentally observed transition from double-hump to single-hump ion density profile when operating at 1.6 and 3 kW.¹³ If at 1.6 kW plasma undergoes

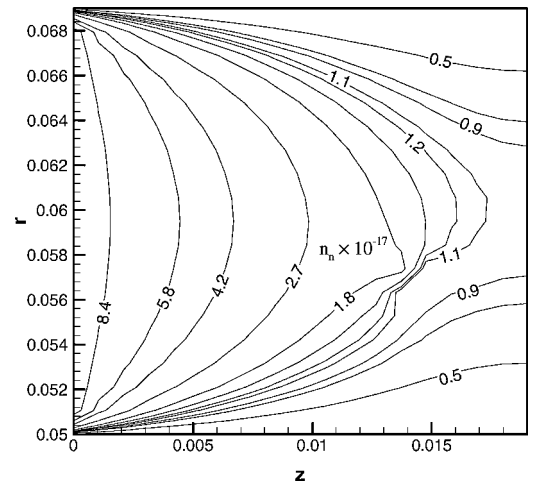


Fig. 3a Neutral number density contours in meters⁻³.

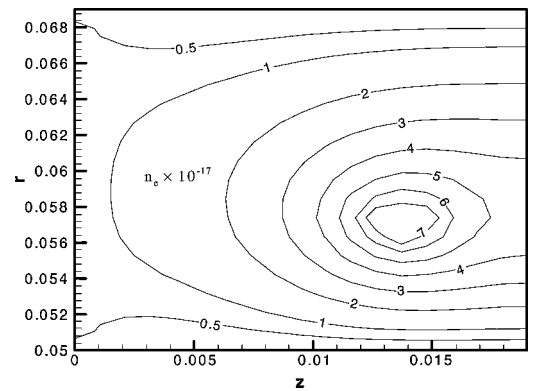


Fig. 3b Plasma number density contours in meters⁻³.

a unique ionization–recombination–ionization cycle, then such behavior should be reflected in the neutral velocity and density profiles. We anticipate that at higher operating powers of the thruster the neutral velocity will exhibit an initial increase (corresponding to the loss of slow neutrals caused by ionization, i.e., number of fast neutrals increase), then a decrease, and again an increase. Also, the neutral number density should exhibit an initial decrease, then an increase, and again a decrease in its number density. It points to the necessity of generalizing the numerical model on the one hand and further experimental investigation of the thruster plasma dynamics on the other hand.

The direction of ion streamlines as plotted in Fig. 4 shows that the ion flow diverges towards the side walls in the downstream section of the channel, indicating the presence of a radial electric field. Haas² has experimentally inferred the presence of this radial field, where the radial asymmetry in the ion number density has been attributed to the presence of such a field. Figure 5 shows that the magnitude of the radial velocity contours increases in the region of strong magnetic field B_r , confirming the experimental observation.² The interaction of ions with the ambient magnetic field could be another possible reason for divergence of the ion streamlines. The magnetic field, which confines the electrons in the azimuthal direction and inhibits their axial motion, can exert its influence on ions as a result of the collisional coupling of ions with the electrons—like ambipolar diffusion in the interstellar plasma.³⁸ Thus, even though ions are not directly coupled to the magnetic field, they can interact with the magnetic field through the electrons. We also anticipate that an additional divergence in the ion beam might appear once the thermal pressure gradient is included in the ion dynamics. When the ion pressure gradient is taken into account, it will give rise to a radial electric field that can cause a dispersion of the accelerated beam. The decollimation of the ion beam in the radial direction will reduce the thrust.

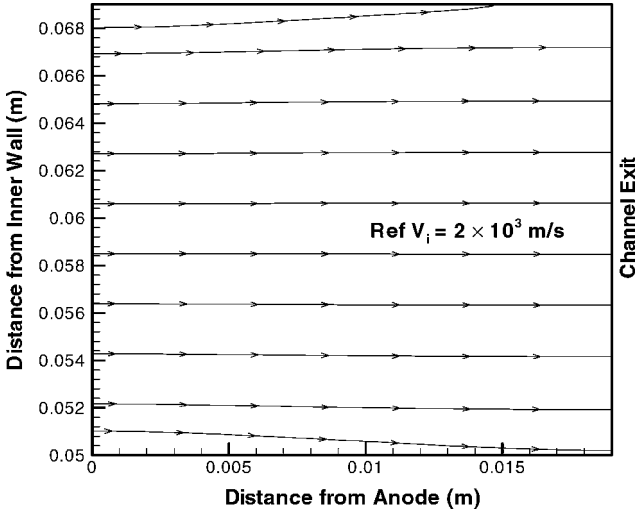


Fig. 4 Directed ion trajectories show the decollimation of ions near the channel exit.

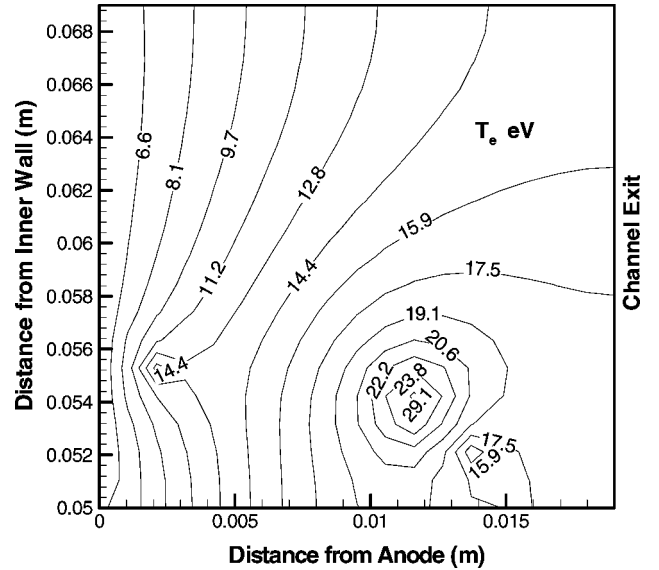


Fig. 6 Electron energy distribution in electron volts.

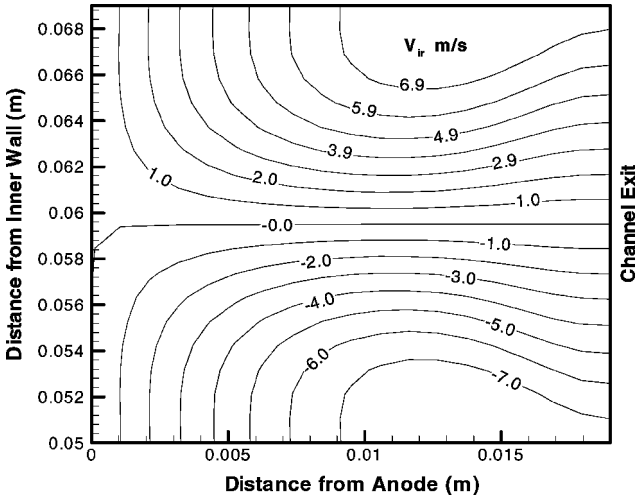


Fig. 5 Radial velocity contours in meters/second.

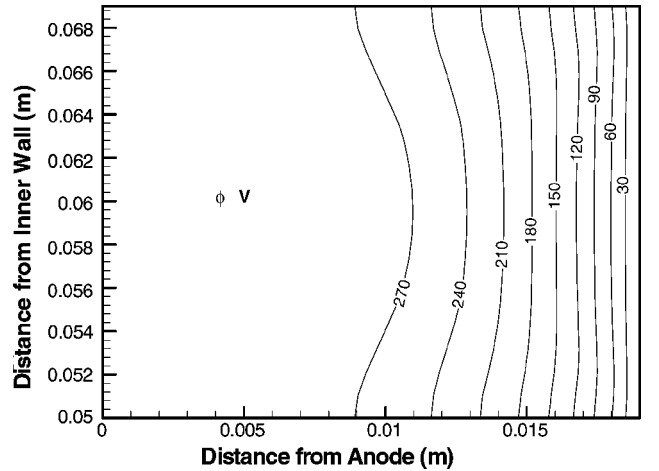


Fig. 7 Potential distribution inside the acceleration channel in volts.

In addition, in the presence of ionization and recombination there is a slight increase in the ion radial velocity near the exit. This increase in the radial velocity could be caused by the depletion of the slow ions to the walls. However, a definite correlation between the velocity and density can only be made if plasma-wall interactions are also included in the model. Recent numerical studies²⁰ suggest that plasma-wall interaction can affect the plasma density, near the exit plane.

Figure 6 describes the electron temperature contours. We note that the increase in the temperature is not uniform in the channel. The maximum increase of ~ 28 eV occurs just downstream of the center of channel towards the inner wall. The peak in the temperature can be attributed to the Ohmic heating caused by the maximum gyration energy in this region. The rise in temperature is similar to the measured electron temperature near the exit of the 1.6-kW class thruster of Haas and Gallimore.¹³ However, the experimental electron temperature peak is spread along a radial line concentrated near the channel exit. Our numerical electron temperature results do not clearly reproduce this profile and can point to the limitation of the present model. Secondary electron emission, ion sputter yield, the electron near-wall conductivity, the near-wall sheath effect, etc., can all affect the electron temperature profile. The present model will be extended to include plasma-wall interactions for better benchmarking with the experimental data.

Figure 7 shows the potential contours inside the acceleration channel. The potential is highest at the inlet (near the anode) and is set to

zero at the outlet (near the cathode). This is similar to the numerical approach presented by Haas.² Although the computed potential is set to zero at the channel exit, observations^{2,13,16} indicate that only one-half to one-third of the potential drop actually takes place downstream of the thruster. In this numerical model the full potential drop is forced to occur inside the channel. We further note that the potential inside the channel is very sensitive to the boundary conditions on the plasma velocities. Such effects will be evaluated in more detail in subsequent versions of the model.

In Fig. 8 the plasma number density, electron temperature, plasma potential along with the electric field, and electron gyration energy are given at radial cross section $r = 0.056$ m, centrally located between the outer and the inner wall. We see that the plasma number density exhibits a narrow half-width at full maximum (hwhm) just upstream of $z = 0.1$ m, suggesting a localized ionization region. It was noted by Bishaev and Kim⁵ in one of the early experiments on SPT that a very small ionization region precedes the acceleration zone. Our numerical result is consistent with the experimental observations.^{2,5} The electron temperature T_e profile in Fig. 8 predicts a sharp increase near the inlet and then a gradual rise before reaching the maximum of about 22 eV near the two-third length downstream of the channel. This is not consistent with the trend in plasma density profile. One would expect that the plasma density maximum will coincide with the electron temperature maximum and that the first local maximum in electron temperature at around 14 eV at normalized axial location of 0.11 will be reflected in a

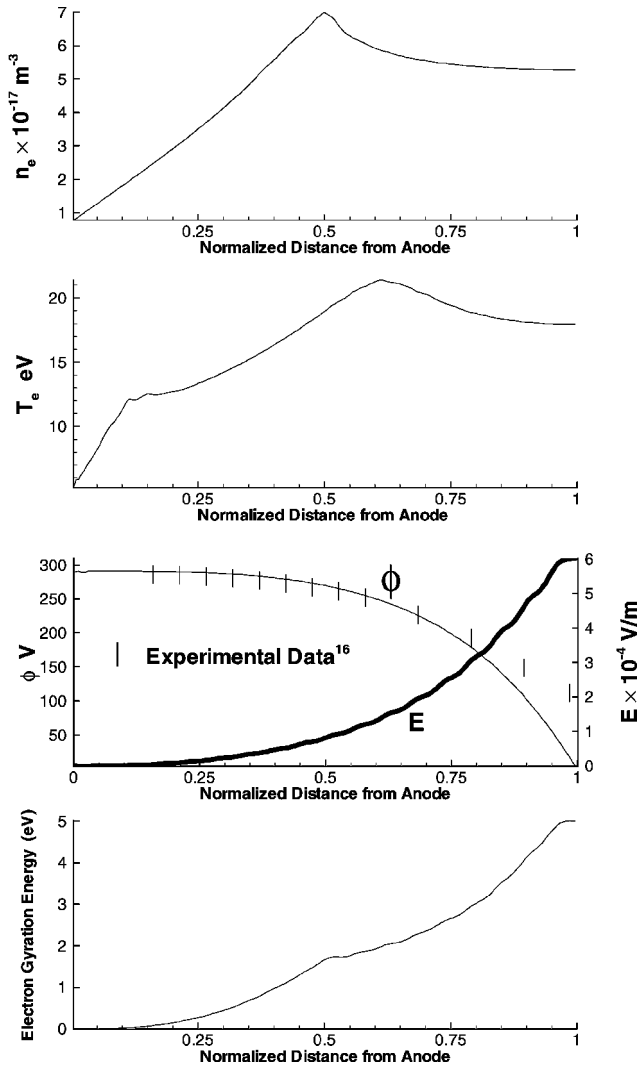


Fig. 8 Distribution of the density, temperature, potential, and gyration energy below the centerline ($r = 0.056$ m) of the acceleration channel.

small peak in the plasma density. However, the first local maximum in the temperature might reflect the loss of slow electrons caused by recombination; because plasma number density is not a sensitive function of source or sink term,¹⁹ the local electron temperature maximum of 14 eV (at $z/L = 0.11$) does not affect the plasma density profile.

The computed potential profile is consistent with the known experimental data (with uncertainty of $-3\text{V}/+6\text{V}$) for a 1.5-kW thruster that operated at 300 V.¹⁶ The potential profile is flat in most of the channel and approaches zero at the exit. Because potential is forced to zero at the exit, the simulation result starts diverging with the experimental result near the exit. The gyration energy (last frame in Fig. 8) displays an increasing trend, reaching maximum near the exit, which agrees well with the published Hall contours^{2,20} that display a maxima upstream of the channel exit for 1.6- and 3-kW-class thrusters. Finally, the thrust at the exit plane of the thruster acceleration channel is calculated via Eq. (24) of Haas and Gallimore.³⁹ The simulation result shows a steady-state thrust of 79.4 mN, which is within the measured data of 95.3 mN and the calculated value of 68 mN at the exit plane of the 1.6-kW thruster.³⁹

V. Conclusions

In this paper a finite element based two-dimensional formulation of partially ionized plasma using multicomponent fluid equation is developed in the presence of ionization and recombination. The model is then applied to study the dynamics inside the Hall thruster. The ion and neutral dynamics are time dependent, whereas

electron dynamics is assumed time independent. By using a third-order electron temperature-dependent polynomial, a self-consistent calculation of the ionization rate has been carried out in the model. Our simulation results suggest that the increase in the plasma number density is correlated with the decrease in the neutral number density. The plasma density prediction is similar to the reported experimental data.^{2,5} There is no significant effect of the ionization and recombination on the plasma number density. This fact is consistent with reported observation.¹⁹

The electron temperature inside the channel shows a gradual increase at the centerline and predicts a hump upstream of the exit at a location between the centerline and the inner wall, which is in agreement with the experimental observation² that shows a peak next to the exit for a 1.5-kW-class thruster. The potential profile agrees with recent experimental studies.¹⁶ The ion streamlines suggest that ions are primarily accelerated because of the axial electric field and reach the maximum velocity near the exit plane. The ions are moving towards the side walls near the thruster exit, indicating the presence of a finite radial electric field. Experimental data² confirm the presence of such a radial electric field. The numerical results are very sensitive to boundary conditions. In the present simulation a choked-exit boundary condition has been imposed on the ion velocity. It needs to be relaxed. The ion velocity reaches the sonic velocity well inside the thruster. Therefore, boundary condition issues require a detailed investigation. The present fluid model also requires further generalization to include plasma-wall interactions. The effect of inelastic processes, namely, secondary emission and sputter yield, should be incorporated. Also, proper modeling of the plasma-sheath dynamics is necessary.

Acknowledgments

This work is supported by NASA Research Grant NAG3-2520 with David Jacobson as the technical monitor. The authors gratefully acknowledge the support of the Electric Propulsion group of NASA Glenn Research Center for providing magnetic field data used in this work.

References

- Zurin, V. V., Kaufman, H. R., and Robinson, R. S., "Physics of Closed Drift Thrusters," *Plasma Sources Science and Technology*, Vol. 8, No. 1, 1999, pp. R1-R20.
- Haas, J. M., "Low-Perturbation Interrogation of the Internal and Near Field Plasma Structure of a Hall Thruster Using a High-Speed Probe Positioning System," Ph.D. Dissertation, Dept. of Aerospace Engineering, Univ. of Michigan, Ann Arbor, 2001.
- Choueiri, E. Y., "Plasma Oscillations in Hall Thruster," *Physics of Plasmas*, Vol. 8, No. 4, 2001, p. 1411.
- Jankovsky, R., Tverdokhlebov, S., and Manzella, D., "High Specific Impulse Hall Thruster Technology," AIAA Paper-99-2949, June 1999.
- Bishaev, A. M., and Kim, V., "Local Plasma Properties in a Hall Current Accelerator with an Extended Acceleration Zone," *Soviet Physics, Technical Physics*, Vol. 23, No. 9, 1978, pp. 1055-1057.
- Kim, V., "Main Physical Features and Processes Determining the Performance of Stationary Plasma Thrusters," *Journal of Propulsion and Power*, Vol. 14, No. 5, 1998, p. 736.
- Komurasaki, K., and Arakawa, Y., "Two-Dimensional Numerical Model of Plasma Flow in a Hall Thruster," *Journal of Propulsion and Power*, Vol. 11, 1995, pp. 1317-1323.
- Fife, J. M., "Hybrid Pic Modeling and Electrostatic Probe Survey of Hall Thrusters," Ph.D. Dissertation, Massachusetts Inst. of Technology, Cambridge, MA, 1998.
- Boeuf, J. P., and Garigues, L., "Low Frequency Oscillations in a Stationary Plasma Thrusters," *Journal of Applied Physics*, Vol. 84, No. 7, 1998, p. 3541.
- Fruchtman, A., and Fisch, N., "Modeling of a Hall Thruster," AIAA Paper 98-3500, July 1998.
- Guerrini, G., and Michaut, C., "Characterization of High Frequency Oscillations in a Small Hall-Type Thruster," *Physics of Plasmas*, Vol. 6, No. 1, 1999, p. 343.
- Morozov, A. I., and Savelyev, V. V., "Fundamental of Stationary Plasma Thruster Theory," *Reviews of Plasma Physics*, Vol. 21, edited by B. B. Kadomtsev and V. D. Shafranov, Consultants Bureau, New York, 2000, p. 261.

- ¹³Haas, J. M., and Gallimore, A. D., "An Investigation of Internal Ion Number Density and Electron Temperature Profiles in a Laboratory-Model Hall Thruster," AIAA Paper 00-3422, July 2000.
- ¹⁴Katz, I., Mandell, M., and Mikellides, Y., "1-D HET Code," Maxwell Tech., Internal Memo to D. Manzella, Cleveland, 2000.
- ¹⁵Litvak, A. A., and Fisch, N. J., "Resistive Instabilities in Hall Current Plasma Discharge," *Physics of Plasmas*, Vol. 8, No. 2, 2001, p. 648.
- ¹⁶Haas, J. M., and Gallimore, A. D., "Internal Plasma Potential Profiles in a Laboratory-Model Hall Thruster," *Physics of Plasmas*, Vol. 8, No. 2, 2001, p. 652.
- ¹⁷Fruchtman, A., Fisch, N. J., and Raitses, Y., "Control of the Electric Field Profile in the Hall Thruster," *Physics of Plasmas*, Vol. 8, No. 3, 2001, p. 1048.
- ¹⁸Ahedo, E., Martinez, P., and Martinez-Sanchez, M., "One-Dimensional Model of the Plasma Flow in a Hall Thruster," *Physics of Plasmas*, Vol. 8, No. 6, 2001, p. 3058.
- ¹⁹Choueiri, E., "Fundamental Difference Between the Two Hall Thruster Variants," *Physics of Plasmas*, Vol. 8, No. 11, 2001, p. 5025.
- ²⁰Keidar, M., Boyd, I. D., and Beilis, I. I., "Plasma Flow and Plasma-Wall Transition in Hall Thruster Channel," *Physics of Plasmas*, Vol. 8, No. 12, 2001, p. 5315.
- ²¹Smith, T. B., Herman, D. A., Gallimore, A. D., and Drake, R. P., "Deconvolution of Axial Velocity Distributions from Hall Thruster LIF Spectra," International Electric Propulsion Conference, Paper IEPC-01-019, Oct. 2001.
- ²²Roy, S., and Pandey, B. P., "Development of a Finite Element Based Hall Thruster Model for Sputter Yield Prediction," *Proceedings of the 27th International Electric Propulsion Conference*, Electric Rocket Propulsion Society, Worthington, OH, Oct. 2001.
- ²³Gascon, N., Meezan, N. B., and Cappelli, M. A., "Low Frequency Plasma Wave Dispersion and Propagation in Hall Thrusters," International Electric Propulsion Conference, Paper IEPC-01-56, Oct. 2001.
- ²⁴Hargus W. A., Jr. and Cappelli, M. A., "Interior and Exterior Laser Induced Fluorescence and Plasma Measurements Within a Hall Thruster," *Journal of Propulsion and Power*, Vol. 18, No. 1, 2002, p. 159.
- ²⁵Ahedo, E., Gallardo, J. M., and Martinez-Sanchez, M., "Model of the Plasma Discharge in a Hall Thruster with Heat Conduction," *Physics of Plasmas*, Vol. 9, No. 9, 2002, p. 4061.
- ²⁶Roy, S., and Pandey, B. P., "Numerical Investigation of a Hall Thruster Plasma," *Physics of Plasmas*, Vol. 9, No. 9, 2002, p. 4052.
- ²⁷Roy, S., and Pandey, B. P., "Plasma-Wall Interaction Inside a Hall Thruster," *Journal of Plasma Physics*, Vol. 68, No. 4, 2003, p. 305.
- ²⁸Roy, S., and Baker, A. J., "A Nonlinear, Sub-Grid Embedded Finite Element Basis for Accurate Monotone Steady CFD Solutions," *Numerical Heat Transfer—Part B*, Vol. 31, No. 2, 1997, pp. 135–176.
- ²⁹Roy, S., and Baker, A. J., "A Nonlinear, Sub-Grid Embedded Finite Element Basis for Accurate Monotone Steady CFD Solutions—Part II, Navier–Stokes Solutions," *Numerical Heat Transfer—Part B*, Vol. 33, No. 1, 1998, pp. 5–36.
- ³⁰Mitchner, M., and Kruger, C. H., *Partially Ionized Gases*, Wiley-Interscience, New York, 1973.
- ³¹Gulczynski, F. S., III, "Examination of the Structure and Evolution of Ion Energy Properties of a 5 kW Class Laboratory Hall Effect Thruster at Various Operational Conditions," Ph.D. Dissertation, Dept. of Aerospace Engineering, Univ. of Michigan, Ann Arbor, 1999, p. 142.
- ³²Golant, V. E., Zhilinsky, A. P., and Sakharov, I. E., *Fundamentals of Plasma Physics*, Wiley, New York, 1977, p. 66.
- ³³Pullins, S., Chiu, Y., Levandier, D., and Dressler, R., "Ion Dynamics in Hall Effect and Ion Thrusters: $\text{Xe}^+ + \text{Xe}$ Symmetric Charge Transfer," AIAA Paper 2000-0603, *38th Aerospace Sciences Meeting and Exhibit*, AIAA, Reston, VA, 2000.
- ³⁴Spitzer, L., *Physics of Fully Ionized Gases*, Wiley-Interscience, New York, 1962, p. 35.
- ³⁵Roy, S., "Combining Galerkin Matrix Perturbation with Taylor Weak Statement Algorithms," *Computer Methods in Applied Mechanics and Engineering*, Vol. 184, No. 1–2, 2000, pp. 87–98.
- ³⁶Balagangadhar, D., and Roy, S., "Design Sensitivity Analysis and Optimization of Steady Fluid-Thermal Systems," *Computer Methods in Applied Mechanics and Engineering*, Vol. 190, No. 42, 2001, pp. 5465–5479; also "Erratum," Vol. 191, No. 3–5, pp. 509, 510.
- ³⁷Richtmyer, R. D., and Morton, K. W., *Difference Methods for Initial-Value Problems*, 2nd ed., Wiley-Interscience, New York, 1967.
- ³⁸Spitzer, L., *Physical Processes in the Interstellar Medium*, Wiley, New York, 1978.
- ³⁹Haas, J. M., and Gallimore, A. D., "An Investigation of Internal Ion Number Density and Electron Temperature Profiles in a Laboratory-Model Hall Thruster," AIAA Paper 2001-3507, July 2001.

Technical Note

TECHNICAL NOTES are short manuscripts describing new developments or important results of a preliminary nature. These Notes cannot exceed 6 manuscript pages and 3 figures; a page of text may be substituted for a figure and vice versa. After informal review by the editors, they may be published within a few months of the date of receipt. Style requirements are the same as for regular contributions (see inside back cover).

Stand-Alone Scheme of Open-Cycle Magnetohydrodynamic Power Generation System

Naoyuki Kayukawa* and Yongming Wang†
Hokkaido University, Sapporo, 060-8628 Japan

Nomenclature

g	=	CO–H ₂ molar ratio
h_j	=	enthalpy of species j , kJ/kmol
n_j	=	molar number of species j , kmol
Q	=	heat, kJ
W	=	work, kJ
α	=	heat split fraction to the gasifier
ΔH_{fj}^0	=	standard formation enthalpy of species j , kJ/kmol
δ	=	heat split fraction to steam
η	=	efficiency

Subscripts

com	=	combustion
comp	=	compression
FP	=	fuel preheater
gf	=	gasifier
IS	=	iodine–sulfur process
LOX	=	oxygen liquefaction
M	=	magnetohydrodynamic generator
ph	=	preheated
S	=	steam
sep	=	CO ₂ separator
t	=	turbine in CO ₂ separation process
(1), (2)	=	inlet, exit

I. Introduction

DURING the period 1984–1993, the U.S. Department of Energy carried out a research and development program of a coal-fired magnetohydrodynamic (MHD) retrofit of existing coal power plants.¹ The major objectives of the proof-of-concept (POC) program were reduced cost of electricity generation and environmental benefits of reduced SO₂ emission. Almost all of the goals of the program were met for integrated topping² and bottoming cycle³ MHD subsystems. Unfortunately, it was found that technological and economical risks from an electric utility's viewpoint remained unanswered.

Received 25 September 2002; revision received 29 April 2003; accepted for publication 29 April 2003. Copyright © 2003 by the American Institute of Aeronautics and Astronautics, Inc. All rights reserved. Copies of this paper may be made for personal or internal use, on condition that the copier pay the \$10.00 per-copy fee to the Copyright Clearance Center, Inc., 222 Rosewood Drive, Danvers, MA 01923; include the code 0748-4658/03 \$10.00 in correspondence with the CCC.

*Professor, Center for Advanced Research of Energy Technology, Kita-ku, Kita 13, Nishi 8; kayukawa@qe.eng.hokudai.ac.jp. Member AIAA.

†Ph.D. Student, Center for Advanced Research of Energy Technology, Kita-ku, Kita 13, Nishi 8.

We feel the technological problems were difficult to solve because of inherent problems with coal slag. Coal slag is incompatible with the regenerative air heater and increases the electrochemical stress in the anode wall. The electrochemical stress in the anode wall chiefly governs the channel durability. Furthermore, Hall field shorting and current leakage are the major consequences of slag polarization, and cathode phenomena played a major role in the degradation of the electrical output performance. The net result of these combined effects was the degradation of both channel durability and output performance.

The coal combustion gas containing slag vapor radiates a large radiation continuum resulting in decrease in temperature, which results in lower electrical conductivity. The low-conductivity plasma requires a sizable channel and superconducting magnet. The value of the power density divided by the magnetic flux density squared in the POC MHD 1A4 channel design⁴ was approximately 0.69 MWe/m³ · T². This value was about half of the 1.44-MWe/m³ · T² value associated with the clean fuel-fired HPDE channel.⁵

Natural gas-fired MHD research in the former U.S.S.R. has resulted in the planning and component construction of the first commercial MHD–steam combined plant U-500. Unfortunately the plant has not been completed because of the drastic change in social and economical situations in the former U.S.S.R. The serious problem of low conductivity, even in a gas-fired plasma, resulted in a massive design to increase efficiency. The U-500 final design, for instance, required a channel length of 20 m with a superconducting magnet weighing 5000 tons (Ref. 6). The design of a base-load-type, open-cycle MHD power generator should be directed at slag-free operation using elevated combustion temperatures. Because of its abundance, coal should be the desired fuel for future fossil-based electrical power generation.

II. Design Concept for an Efficient Thermal Cycle

Both steam generation and air preheating comprised the basic regeneration concept of past MHD power-generation systems. In combined systems, a definite amount of regenerated heat is lost due to the bottoming cycle efficiency characteristics. The benefit of exhaust heat recirculation to the topping combustor is shown in Fig. 1c, comparing a regenerative scheme (Fig. 1a) with a combined cycle (Fig. 1b). The regeneration factor R is defined as the ratio of heat recirculated (regenerative design) or the steam heat (combined design) to the heat input to the regenerator. For the regenerative system, $R = Q_R / [(Q_C + Q_R)(1 - \eta_i)]$ and for the combined system $R = Q_R / [Q_C(1 - \eta_i)]$. Figure 1c shows the total efficiency is greater for the regenerative system compared to the combined system under high regeneration factors. Both systems have the same topping converter efficiency η_t and fuel heat input Q_C . The regenerative system under these conditions is less dependent on the topping converter efficiency. It is also clear from the energy conservation law that the combustion temperature in the regenerative system is much higher than in the combined system.

III. Stand-Alone Scheme of the MHD System

We consider three sequential processes for regeneration of MHD exhaust enthalpy over a wide temperature range. The first process

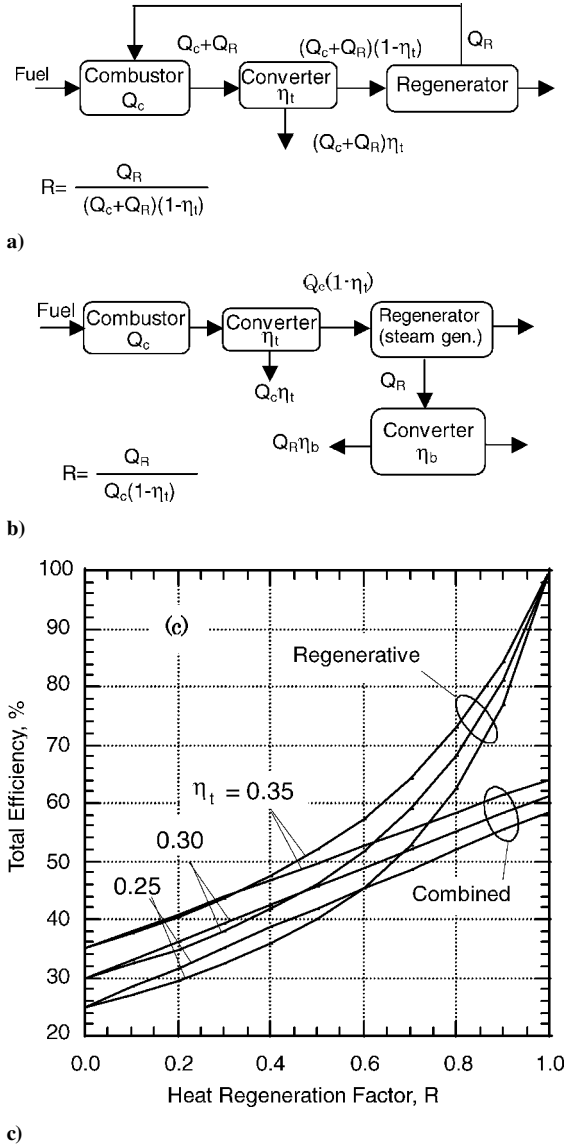
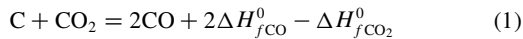


Fig. 1 Energy flow schematics in a) regenerative b) combined systems and c) energy efficiency characteristics.

is the high-temperature thermochemical gasification of coal as described by



where the heat of the reaction is estimated using standard heat of formation enthalpies for j species ΔH_{fj}^0 . The heat of reaction is supplied from the exhaust heat of recirculated syngas-oxygen combustion products coming from the diffuser. The second is the syngas preheating with a recuperative-type heat exchanger applied to the slag-free syngas/ CO_2 / H_2O gas mixture in a temperature range of approximately 1300–2000 K. The third regeneration process useful below 1300 K is the iodine-sulfur process, proposed by Norman et al.⁷ The iodine-sulfur (IS) process is an innovative water-splitting reaction described by $I_2 + SO_2 + 2H_2O = H_2SO_4 + 2HI$, $2HI = H_2 + I_2$ and $H_2SO_4 = H_2O + SO_2 + 1/2O_2$. The overall reaction can be considered as a water decomposition process, $H_2O = H_2 + 1/2O_2$, with heat absorption of 13.8×10^3 kJ/kmol. We consider that the heat can be supplied from the exhaust coming out from the fuel preheater. The advantage of the IS process is that the sulfur and iodine chemicals circulate in closed loops and no pollutants are exhausted into the atmosphere. The IS process is under development for hydrogen

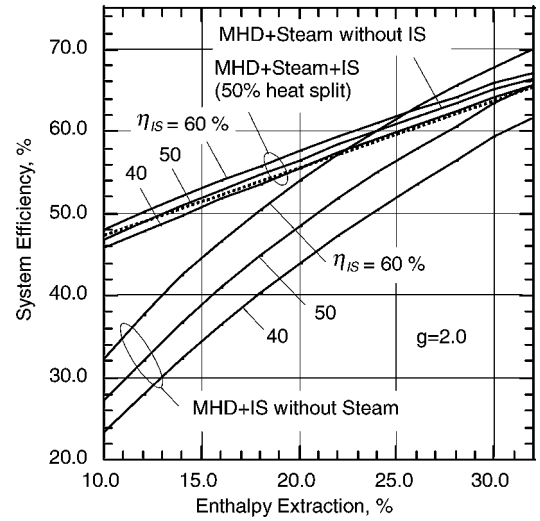


Fig. 2 Efficiency of stand-alone MHD system as functions of channel enthalpy extraction and IS efficiency and the effect of heat splitting to steam cycle for temperature regulation.

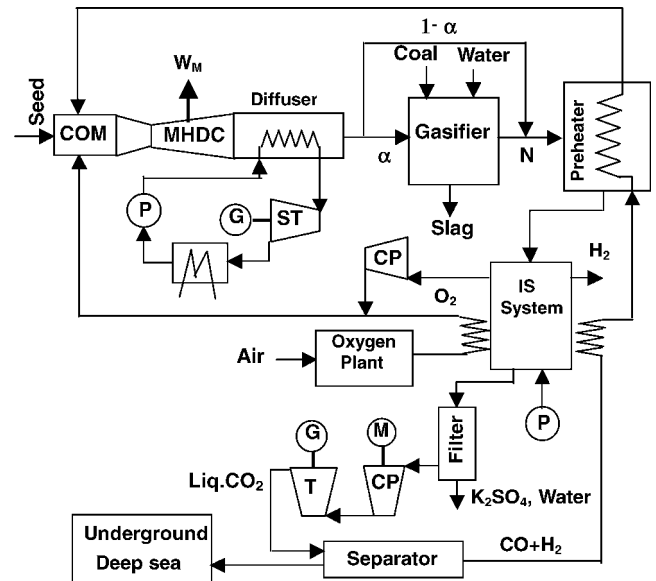


Fig. 3 Layout of an MHD stand-alone system with CO_2 liquefaction and steam cycle for combustion temperature regulation.

production purposes with heat from a high-temperature gas-cooled nuclear reactor at the Japan Atomic Energy Research Institute.⁸

A distinctive feature of the stand-alone MHD system is that a considerable amount of energy can be recirculated to the combustor as chemical energy and latent heat of the fuel. In fact, the combustion temperature could possibly become too high for practical combustor design, and it may be necessary to split some fraction of the MHD heat for steam generation. Although this diverted fraction may lower the overall efficiency characteristics, its role is primarily to operate within the practical limit of combustion temperature. The heat splitting does not always lower the overall efficiency, as seen in Fig. 2.

The proposed stand-alone MHD power generation system is shown in Fig. 3. The steam generator is just downstream of the MHD generator. An appropriate fraction $(1 - \alpha)$ of the MHD exhaust should bypass the gasifier and be mixed with syngas products before the preheater. The fractional split is necessary to match the gasifier exit temperature to the coal ash melting temperature, because there is a definite temperature drop in the gasification process. H_2O and K_2SO_4 particulates are separated from the syngas in the filter stage. No seed regeneration process is considered in the present

system to minimize the ambiguity in the energy balance calculation and to compare the results with those of the previous works⁹ on an MHD combined scheme. Syngas is separated from CO₂ in the CO₂ separation unit comprising a compression and an air-turbine-type expansion processes. The syngas is preheated by IS-exhaust heat to 355 K, mixed with hydrogen from the IS system, and then heated higher in the recuperative heater. The heated syngas is recirculated to the combustor where the combustion is performed with oxygen for efficient CO₂ separation. The combustor pressure is fixed at 0.75 MPa, under which the channel enthalpy extraction ranges up to approximately 31.2–34.4% with fixed channel exit pressure at 0.2 MPa.

In actual system design studies, some modifications should be taken into account for regeneration of cooling heat from high-temperature components, for instance, the regeneration scheme for feed water heating and/or for liquid oxygen vaporization. The modification may result in about the same system performance as estimated under the adiabatic wall conditions. We neglect all heat losses in the present paper, as well as from the comparison purpose of the present results with those of the MHD combined system studies in Ref. 9.

IV. Estimation of Efficiencies

The IS process efficiency, as defined by the ratio of the hydrogen chemical energy to the heat input, is presently, 40–45% (Ref. 10). Also, the IS process has a much higher efficiency capability with modification of elemental processes.¹¹ By definition, the hydrogen production for a given IS efficiency can be written as

$$n_{\text{H}_2}^{\text{IS}} = \eta_{\text{IS}} Q_{\text{IS}}^{(1)} / (-\Delta H_{f\text{H}_2\text{O}}^0) \quad (3)$$

where $Q_{\text{IS}}^{(1)}$ is the heat input to the IS system. For the gasification process, we assume the carbon input is 1 kmole. Assuming that all carbon is gasified by reactions (1) and (2) with fixed compositions at the exit, we obtain gaseous molar numbers: $n_{\text{CO}}^{\text{gf}(2)} = G_{\text{C}}$, $n_{\text{H}_2}^{\text{gf}(2)} = G_{\text{H}}$, $n_{\text{CO}_2}^{\text{gf}(2)} = G_{\text{C}}\alpha - 1/2(G_{\text{C}} - G_{\text{H}})$, $n_{\text{H}_2\text{O}}^{\text{gf}(2)} = (G_{\text{H}} + n_{\text{H}_2}^{\text{gf}(2)})\alpha - G_{\text{H}} + n_w$, where the superscript gf(2) denotes the gasifier exit, g is the molar ratio of CO division H₂ in the syngas, $G_{\text{C}} = 2g(g+1)^{-1}$, $G_{\text{H}} = 2g(g+1)^{-1}$, and n_w is the water molar number injected into the gasifier for H₂O balance. Because fuel input to the MHD combustor is equal to $n_{\text{CO}}^{\text{gf}(2)}$ plus $n_{\text{H}_2}^{\text{gf}(2)} + n_{\text{H}_2}^{\text{IS}}$, and the oxidizer is pure oxygen, the split molar numbers that bypass the gasifier are $n_{\text{CO}_2} = G_{\text{C}}(1-\alpha)$ and $n_{\text{H}_2\text{O}} = (G_{\text{H}} + n_{\text{H}_2}^{\text{IS}})(1-\alpha)$. Then, on mixing at the point N (see Fig. 3), the gas components at the preheater inlet can be given by $n_{\text{CO}}^{\text{FP}(1)} = G_{\text{C}}$, $n_{\text{H}_2}^{\text{FP}(1)} = G_{\text{H}}$, $n_{\text{CO}_2}^{\text{FP}(1)} = 1.0$, and $n_{\text{H}_2\text{O}}^{\text{FP}(1)} = n_{\text{H}_2}^{\text{IS}} + n_w$. The oxygen molar number is one-half of the total fuel molar number, of which we assume $n_{\text{H}_2}^{\text{IS}}/2$ is supplied by the output of the IS system and $(G_{\text{C}} + G_{\text{H}})/2$ is supplied from a liquid O₂ storage unit. The oxygen storage unit operates at 140 K and 3.0 MPa.

With the given molar numbers, the gasification heat absorbed as chemical energy is estimated as $Q_a = (2\Delta H_{f\text{CO}}^0 - \Delta H_{f\text{CO}_2}^0)(G_{\text{C}} - G_{\text{H}})/2 + (\Delta H_{f\text{CO}}^0 - \Delta H_{f\text{H}_2\text{O}}^0)G_{\text{H}}$. We suppose that the syngas preheat temperature is given by $T_{\text{ph}}^{(2)} = T_{\text{FP}}^{(1)} - \delta T$, where $T_{\text{FP}}^{(1)}$ is the mixed gas temperature at the point N . If δT is much less than $T_{\text{FP}}^{(1)}$, then preheated syngas enthalpy can approximately be given by $h_j^{\text{ph}(2)} = h_j(T_{\text{FP}}^{(1)}, p) - (\partial h_j / \partial T)_{T_{\text{FP}}^{(1)}} \delta T$ where $j = \text{CO}$, and H₂ and p is the fuel pressure in the preheater. Estimating the heat input to the IS system from Eq. (3), we obtain α , $T_{\text{FP}}^{(1)}$, and $n_{\text{H}_2}^{\text{IS}}$ by solving the following three energy balance equations applied to the gasifier, the point N , and the preheater:

$$(1 - \eta_M)(1 - \delta)\alpha Q_M = Q_a + Q_{\text{slag}} + Q_{\text{gf}}^{(2)} + h_w^v n_w \quad (4)$$

$$(1 - \eta_M)(1 - \delta)Q_M(1 - \alpha) + Q_{\text{gf}}^{(2)} = Q_{\text{ph}}^{\text{net}} + \eta_{\text{IS}}^{-1}(-\Delta H_{f\text{H}_2\text{O}}^0)n_{\text{H}_2}^{\text{IS}} \quad (5)$$

$$(1 - \eta_M)(1 - \delta)Q_M(1 - \alpha) + Q_{\text{gf}}^{(2)} = Q_{\text{FP}}^{(1)} \quad (6)$$

here η_M is the MHD channel enthalpy extraction ratio, $\delta \equiv Q_{\text{S}}/(1 - \eta_M)Q_M$ is the fraction of steam heat to the input heat, and h_w^v is the molar water vaporization heat at the saturation pressure equal to the gasifier pressure, which is assumed to be 0.2 MPa. Q_{slag} is the heat loss accompanying slag rejection, and $Q_{\text{ph}}^{\text{net}}$ is the net heat transferred to fuel in the preheater as given by

$$Q_{\text{ph}}^{\text{net}} = G_{\text{C}}(h_{\text{CO}}^{\text{ph}(2)} - h_{\text{CO}}^{\text{ph}(1)}) + (G_{\text{H}} + n_{\text{H}_2}^{\text{IS}})(h_{\text{H}_2}^{\text{ph}(2)} - h_{\text{H}_2}^{\text{ph}(1)}) \quad (7)$$

The outlet enthalpies should be estimated at $T_{\text{FP}}^{(1)} - \delta T$ using a combustor pressure of 0.75 MPa being equal to the combustor pressure. As for the preheater inlet enthalpies of CO and H₂ in Eq. (7), we assume 355 K and 1.0 MPa. Q_M in Eqs. (4–6) is the total heat input to the MHD channel represented by the sum of the combustion heat, the fuel preheat, and the oxygen heat, $Q_M = Q_{\text{com}} + Q_{\text{ph}} + Q_{\text{O}_2}$. Here,

$$Q_{\text{O}_2} = (n_{\text{H}_2}^{\text{IS}} + G_{\text{C}} + G_{\text{H}})h_{\text{O}_2}$$

$$Q_{\text{ph}} = G_{\text{C}}h_{\text{CO}}^{\text{ph}(2)} + (G_{\text{H}} + n_{\text{H}_2}^{\text{IS}})h_{\text{H}_2}^{\text{ph}(2)}$$

and

$$Q_{\text{com}} = G_{\text{C}}(\Delta H_{f\text{CO}}^0 - \Delta H_{f\text{CO}_2}^0) + (G_{\text{H}} + n_{\text{H}_2}^{\text{IS}})(-\Delta H_{f\text{H}_2\text{O}}^0)$$

The oxygen enthalpy is calculated with the assumption that IS–O₂ is adiabatically compressed from 0.1 to 0.75 MPa, starting from a temperature of 355 K. Also, the oxygen from the liquid storage is vaporized with the heat from the IS system to the same temperature and pressure. When Eqs. (4–6) are solved, the minimum water injection can be determined parametrically by the condition that $n_{\text{H}_2\text{O}}^{\text{gf}(2)} = 0$ at the gasifier exit. We assume the following process for CO₂ separation and liquefaction. The water-free CO, H₂, and CO₂ mixture from the filter at 355 K and 0.1 MPa is first compressed isothermally to 5.0 MPa consuming work W_{sep} and then expands adiabatically in an air-type gas turbine to 1.0 MPa. In the turbine, the temperature drops down to 224 K, which is lower than the CO₂ saturation temperature at 1.0 MPa, but above the saturation temperatures of the CO and H₂ gases. Therefore, CO₂ can be liquefied, and some work W_t , corresponding to CO and H₂ pressure drop, will be extracted. We assume the turbine exit pressure is sufficient to feed the fuel to the MHD combustor through two preheating processes. Using the results of the preceding mass and energy calculations and estimating the steam turbine work as $W_S = \eta_S Q_S$, we obtain the system efficiency as

$$\eta = (\eta_M Q_M + W_S + W_t - W_{\text{sep}} - W_{\text{comp}} - W_{\text{LOX}}) / (-\Delta H_{f\text{CO}_2}^0) \quad (8)$$

where W_{comp} and W_{LOX} are the IS–O₂ compression work and the O₂ production work, which is assumed to be 9.89×10^3 kJ/kmol based on the value for current systems. The pump work for feeding water to the gasifier and the IS system can be neglected.

V. Results

The calculated system efficiency is shown graphically in Fig. 2. The graphs are shown as functions of η_M and η_{IS} with $g = 2$, which is a typical value of CO/H₂ molar ratio in high-temperature thermochemical synthesis with syngas–O₂ combustion products as oxidizers. The efficiency for higher g values becomes slightly higher because energy absorption in reaction (1) is higher than in reaction (2). However, the effect is not appreciable. Figure 2 shows the efficiency comparisons of splitting the heat to the steam cycle, with and without the IS system. The latter efficiency of a thermochemical-type MHD–steam combined cycle with a regenerative-type syngas preheater was reported in previous work.⁹ The steam turbine efficiency, the ratio of steam heat to turbine work, was 48.5 % for the combined case, where the same conditions were assumed for the combustor pressure and the lowest temperature and pressure in the system. Moreover, the same scheme was used for CO₂ separation and liquefaction processes, O₂ production work, with no heat losses from the associated units. We note that the heat split to the steam cycle is favorable when the MHD channel enthalpy extraction is low.

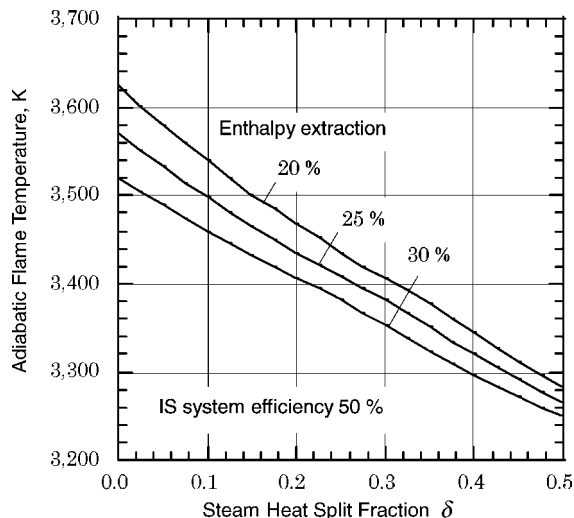


Fig. 4 Adiabatic flame temperatures as function of heat split fraction δ to steam cycle.

On the other hand, much higher efficiencies can be expected when both enthalpy extraction and IS efficiency are high. This tendency can be explained by the characteristics of the regenerative system shown in Fig. 1. The results show that the steam heat split mitigates the effects of the IS efficiency. This is because the IS hydrogen production decreases with the heat split ratio.

A distinctive feature of the CO_2 -free, stand-alone MHD system is its extremely high combustion temperature. This temperature is due to oxygen combustion, efficient chemical and thermal energy regeneration, and recirculation to the topping combustor. When we define the heat amplification factor as the ratio of total channel heat input Q_M to that of the direct carbon combustion ($-\Delta H_{f\text{CO}_2}^0$), its value ranges from 2.3 to 2.8 with $\eta_{\text{IS}} = 40\text{--}60\%$, $\eta_M = 25\%$, and steam split fraction of $\delta = 0$ and 1.56–2.1 with $\eta_{\text{IS}} = 50\%$, $\eta_M = 20\text{--}30\%$, and $\delta = 0.5$. Under given η_M and η_{IS} , the adiabatic flame temperatures can be varied with δ , as shown graphically in Fig. 4. The actual operating temperatures may be a few hundreds degree lower than those shown. However, this result suggests that the open-cycle MHD power generation has a potential for a wide range of selectivity of combustion temperatures. This kind of capability has not been recognized, and such high-temperature MHD power generation technologies have never been explored.

VI. Conclusions

The present results clearly demonstrate that the thermodynamic advantage of an open-cycle MHD generator as a high-temperature

electromagnetic turbine could be achieved in a system of efficient recirculation of exhaust heat. The exploitation of combustion, thermochemical synthesis, and MHD generating technologies, such as further development in high temperature electrode materials starting from the U-500 design basis, at much elevated temperatures, is worthwhile for economical and environmentally acceptable fossil power cycles for clean coal utilization in the future.

References

- ¹Seikel, G. R., Sovie, R. J., Burns, R. K., Barna, G. J., Burkhart, J. A., Naininger, J. J., and Smith, J. M., "A Summary of the ECAS Performance and Cost Results for MHD Systems," *Proceedings of the 15th Symposium on Engineering Aspects of Magneto-hydrodynamics*, SEAM Inc., Philadelphia, Paper III.4, May 1976.
- ²Pian, C. C. P., and Schmitt, E. W., "Results of the Integrated Topping Cycle MHD Generator Testing," *Proceedings of the 32nd Symposium on Engineering Aspects of Magneto-hydrodynamics*, SEAM Inc., Pittsburgh, Session 1 Paper, June 1994.
- ³Atting, R. C., Chapman, J. N., and Johanson, N. R., "Status of Proof-of-Concept Testing at the Coal-Fired-Flow Facility," *Proceedings of the 31st Symposium on Engineering Aspects of Magneto-hydrodynamics*, SEAM Inc., Pittsburgh, Whitefish, Paper II.5, June 1992.
- ⁴Petty, S. W., Dunton, A., Reich, J., and Simpson, W., "1A4 Channel Design and Fabrication," *Proceedings of the 29th Symposium on Engineering Aspects of Magneto-hydrodynamics*, SEAM Inc., Pittsburgh, Paper II.1, June 1991.
- ⁵Starr, R. F., Christensen, L. S., Garrison, G. W., and Whitehead, G. L., "Preliminary Faraday Performance of a Large Magnetohydrodynamic Generator at High Magnetic Field," *Journal of Energy*, Vol. 6, No. 3, 1982, pp. 163–170.
- ⁶Batenin, V. M., and Kiryenin, I. A., "Large Super-Conducting Magnet System Developed by the IVTAN Association of Russian Academy of Sciences," *Proceedings of the Second International Workshop on Super-Conducting Magnets*, StM/Nautilus, Genova, Paper 1.1, Dec. 1994.
- ⁷Norman, J. H., Besenbruch, G. E., and Brown, L. C., "Thermo-Chemical Water Splitting Cycle, Bench Scale Investigations and Process Engineering," GA Rept. GA-A 16713, May 1982.
- ⁸Nakajima, H., Ikenoya, K., Ohnuki, K., and Shimizu, S., "Closed Cycle Continuous Hydrogen Production Test by Thermo-Chemical IS Process," *Kagaku Kogaku Ronbunshyu*, Vol. 24, No. 2, 1998, pp. 352–355.
- ⁹Kayukawa, N., "A New Fossil Power Systems and the Role of Open-Cycle MHD Generators," *Journal of Propulsion and Power*, Vol. 18, No. 4, 2002, pp. 871–879.
- ¹⁰Ohnuki, K., Nakajima, H., Futakawa, M., Ioka, I., and Shimizu, S., "Thermo-Chemical Water Splitting for Hydrogen Production," *Proceedings of the 8th International Topical Meeting on Nuclear Reactor Thermo-Hydraulics*, Japan Society of Mechanical Engineers, Vol. 3, Sept. 1998, pp. 1803–1808.
- ¹¹Oeztuerk, I. T., Hammache, A., and Bilgen, E., "A New Process for Oxygen Generation Step for the Hydrogen Producing Sulphur-Iodine Thermo-Chemical Cycle," *Transactions of the Institution of Chemical Engineers*, Vol. 72, Pt. A: Chemical Engineering Research & Design, March 1994, pp. 241–250.